Chapter 10

Plasmonics on Optical Fiber Platforms

Hyuntai Kim

Additional information is available at the end of the chapter

http://dx.doi.org/10.5772/intechopen.79146

Abstract

Optical fiber platforms are promising for plasmonics research and applications, thanks to their compactness, flexibility, and cost-effectiveness, which are further leveraged by easy accessibility to numerous fiberized sources and devices. In this chapter, the author particularly pays attention to novel surface plasmon polariton (SPP) devices implemented onto optical fiber platforms. First, the author investigates novel circular metallic nanoslit-based optical fiber facets for the generation of axially symmetric SPPs with significantly enhanced noise characteristics. Second, the author investigates novel metallic Fresnel-zone-plate optical fiber facets for super-variable focusing with incident wavelength and for selective focusing with incident polarization. Third, the author investigates novel metal-coated angled optical fiber facets for versatile SPP coupling and its application to wavelength-dependent off-axis beaming, which offer high efficiency, unidirectionality, and perfect compatibility with fiberized light sources. The author expects that these investigations will broaden both fiber optics and plasmonics research fields, and also be useful for various novel applications, including micro-/nanomachining, optical trapping, and biomedical sensing, for example.

Keywords: fiber optics, plasmonic hotspot, optical focusing, surface plasmon coupling, plasmonic lens

1. Introduction

Optical fiber is a strand of transparent dielectric waveguide, which can guide and transmit optical signals with extremely low loss [1, 2]. It has a lot of merits in being used as a platform for the excitation of surface plasmon polariton (SPP), which is the collective oscillation of electrons at a dielectric-metal interface, and for its applications from the perspectives of compactness, flexibility, and cost-effectiveness [1, 3]. Moreover, such merits are further leveraged

by the full accessibility to premium grade fiberized devices already combined with light sources, detectors, and various other components of optical functionalities. Once optical fiber platforms are considered for SPP research and applications, one most apparent effect obtained from them is the fact that the use of free-space optics can be eliminated or minimized as illustrated in **Figure 1**.

In fact, a variety of plasmonic nanostructures implemented onto optical fiber platforms have been investigated to date: Most of them were based on metallic nanostructures constructed on the facet, tip, and polished or tapered side of optical fiber [4–7]. Among them, the author focuses on the optical fiber facet structures in that they inherently provide an easy and efficient access to light that the core of the optical fiber guides. Thus, in this chapter, the author investigates and discusses various optical fiber facet structures for an efficient platform for plasmonics research and applications: First, the author investigates trench-assisted circular metallic nanoslits on flat-cleaved optical fiber facets for the generation of axially symmetric SPP hotspots with significantly enhanced noise characteristics [8]. Second, the author investigates fiberized plasmonic Fresnel zone plates for super-variable focusing with incident wavelength and for selective focusing with incident polarization [9]. Third, the author investigates novel metal-coated angled optical fiber facets for a versatile optical-to-SPP mode converter, which provide high efficiency, unidirectionality, and perfect compatibility with fiberized light sources [10]. The detailed investigation and discussion with numerical and experimental demonstrations are given in the following sections. In addition, it is noteworthy that all the numerical simulations were done based on the finite element method (FEM: COMSOL Multiphysics®), and that all the metallic nanostructures were fabricated based on the electron-beam evaporation method and the focused ion beam (FIB) milling method, unless stated otherwise.

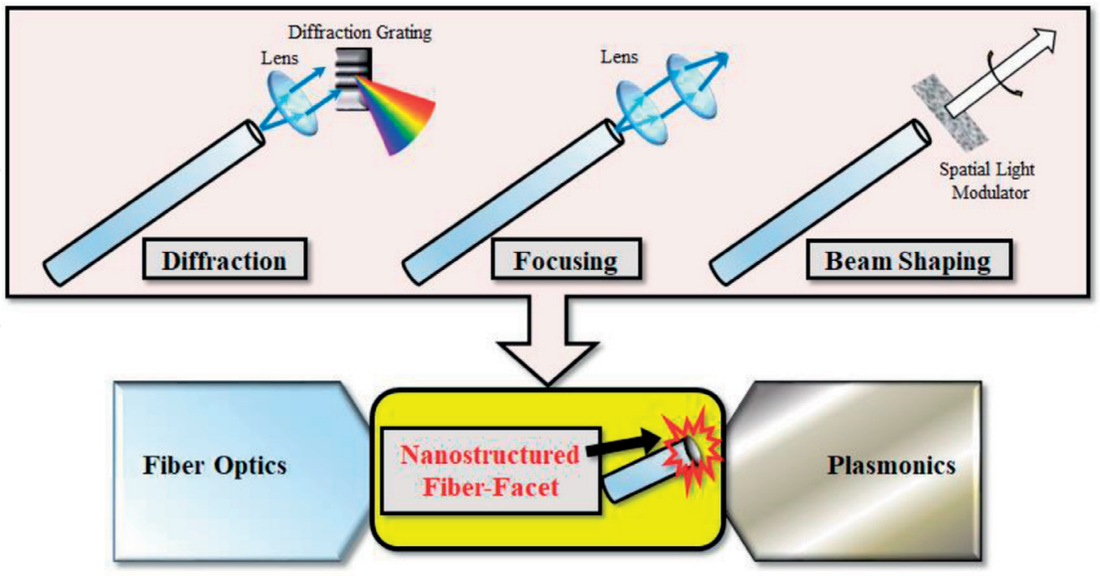

Figure 1. Schematic illustrations of various nanostructured optical fiber facets for plasmonic applications.

2. Trench-assisted circular metallic nanoslits for low-noise plasmonic hotspot generation

Plasmonic focusing is beneficial to diverse novel applications, such as lithography [11], high harmonic generation [12], and sensing [13], etc. To date, various configurations have been suggested for plasmonic focusing, such as nanoparticles [14], circular nanoslits [15], bowtie structures [16], metal tips [17], etc. Among them, circular metallic nanoslits (CMNSs) engraved on a thin metal film are of great interest because of their capability of generating focused cylindrical SPPs (C-SPPs), that is, plasmonic hotspots, via modest fabrication procedures [8]. While various structures and schemes were extensively investigated to intensify the plasmonic hotspots, the effect of nonconfined diffracted light (NCDL) that accompanies C-SPPs has not been investigated rigorously [18]. In most cases of CMNSs, it is hard to avoid the disturbance of NCDL, so that its consequence increases the background noise, thereby degrading the signal-to-noise ratio (SNR) and sharpness of the C-SPP hotspot.

Recently, exploiting the multipole cancelation mechanism (MPCM) proposed for effective noise-canceling [19], the author has investigated novel trench-assisted circular metal nanoslits (TA-CMNSs) implemented onto optical fiber facets [20], where the use of the optical fiber platform leads to considerably simplified procedures to excite C-SPPs with low noise [21].

In this section, the author discusses the characteristics of TA-CMNS structures implemented on a metal-coated optical fiber facet and shows that they can have substantially improved SNR characteristics based on the MPCM. In particular, these structures are useful for plasmonic devices that particularly require high SNR characteristics, such as bio-sensing, imaging, surface-enhanced Raman spectroscopy, etc.

2.1. Fiberized circular metallic nanoslits

Different from one-dimensional nanoslits, a CMNS generates a plasmonic hotspot at its center by two-dimensionally focusing the inward-propagating C-SPP, so that the hotpot can be intensified to a substantial level. Moreover, its efficiency can also be enhanced if radially polarized light is utilized [22]. Indeed, the use of the optical fiber platform for CMNS applications can bring in a considerable advantage, because radially polarized fiber-optic modes (e.g., TM_{01} mode) are readily accessible.

A full-vectorial simulation of a CMNS constructed on top of an optical fiber facet is considered in the following, which was initially proposed and analyzed in [8]. It was assumed that the optical fiber had a step-index core with a diameter of 8 μm and a numerical aperture (NA) of 0.1, and that the metal was made of gold, the material parameters of which, that is, the refractive index and extinction coefficient, were given by $n = 0.16918$ and $k = 3.8816$, respectively. The wavelength of incident light was set as $\lambda = 700$ nm. The width of the slit and the thickness of the metal layer were set to 87.5 nm and 500 nm, respectively. The annular slit was concentric with the fiber core. In particular, the radius of the annular slit was matched with the

intensity distribution of the TM_{01} mode of the optical fiber in order to maximize the modefield overlap with the opening of the annular slit.

First of all, a simple CMNS without having any trench structure was numerically analyzed [8]. The C-SPP (graded red/yellow) and NCDL (graded blue) field intensity patterns are illustrated in **Figure 2**. It is shown that while a plasmonic hotspot was formed at the center of the metal surface, the NCDL was also focused at the same position of the hotspot. In particular, the NCDL component at the center was hardly distinguishable with the C-SPP signal, so that the SNR (defined as the ratio of the C-SPP intensity to the NCDL intensity) of the device was inevitably degraded. The peak and mean SNRs within the central main lobe of the C-SPP hotspot were given by 22.74 and 14.70 dB, respectively.

2.2. Noise cancelation in trench-assisted CMNSs

As discussed in the preceding section, NCDL tends to be overlapped with the C-SPP hotspot. In particular, the NCDL propagating in the direction parallel to the metal surface can considerably degrade the SNR of the C-SPP hotspot. Thus, to improve the SNR, NCDL should be suppressed. As proposed in [8], a trench-assisted (TA) structure along with the conventional CMNS can be considered in order for minimizing the disturbance incurred by the unwanted NCDL. The proposed TA-CMNS structure and its operation principle are illustrated in **Figure 3**. The main strategy of exploiting the TA structure is such that a considerable portion of the primary NCDL (depicted in blue) from the slit is canceled out by the secondary NCDL (depicted in red) excited by the TA structure alongside the slit. The TA-CMNS was in fact designed in a way that the secondary NCDL destructively interferes with the primary NCDL, as shown in **Figure 3**. It should be further noted that the trench structure having a sharp edge at P_2 is

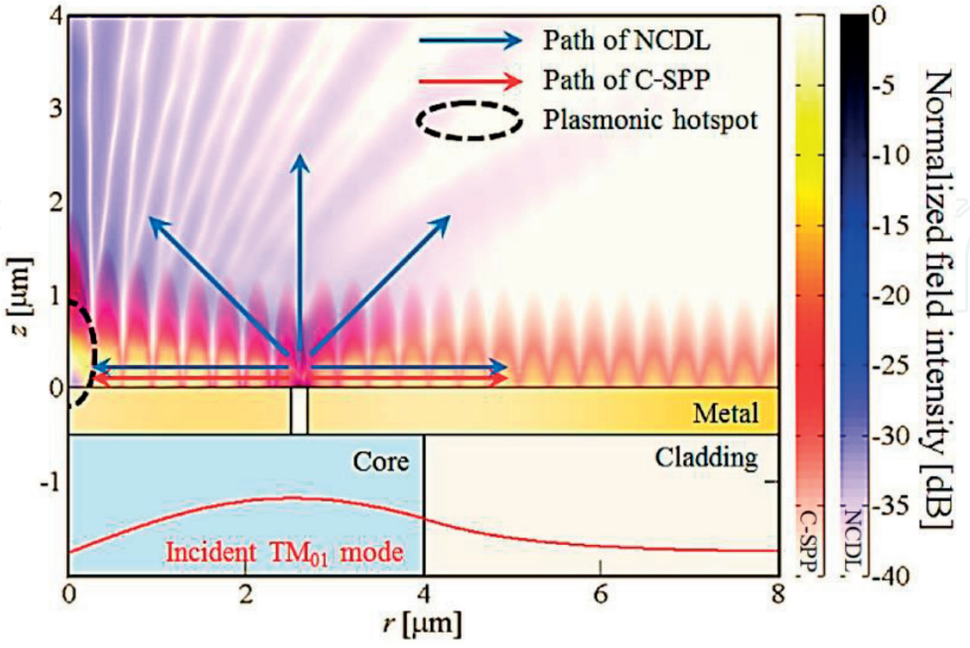

Figure 2. Relative field intensity patterns in dB calculated for a simple CMNS with TM_{01} optical fiber mode incidence [8].

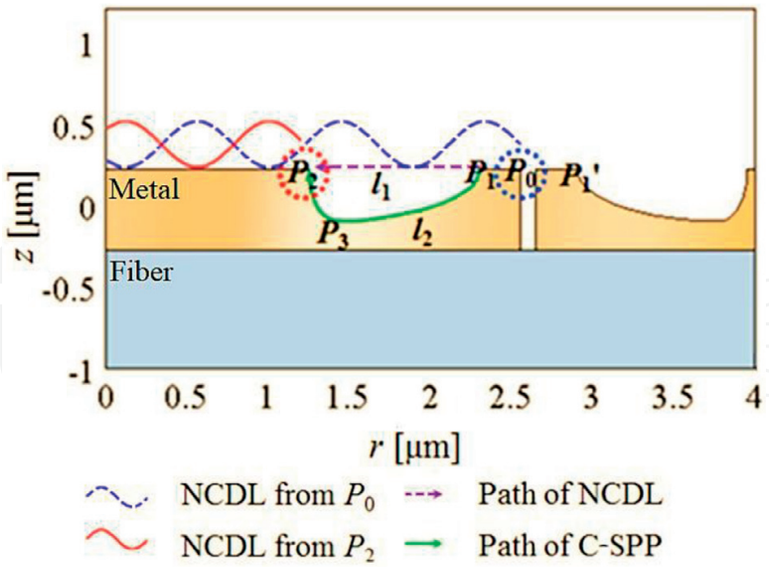

Figure 3. Schematic of a TA-CMNS and its operation principle [8].

preferred, because P_2 is the location where charges are predominantly induced [14], so that it can be regarded as a "quasi-pole source" that generates secondary NCDL [8].

In order to make the primary NCDL and the secondary NCDL out of phase completely, the phase difference between the primary NCDL (path l_1) and the C-SPP (path l_2) should be an odd integral multiple of λ, because the phase of the secondary NCDL is mostly determined by the phase of the C-SPP, such that [8].

$$\mathrm{Re}(k_{C-SPP})l_2 - kl_1 = (2m-1)\pi, \tag{1}$$

where k and k_{C-SPP} denote the wavenumbers of the NCDL and the C-SPP, respectively, Re the real part of the argument, and m an integer number. In addition, the location P_1 should also be determined carefully in order that the cavity formed between the two inner edges of the trench P_1 and P_1' satisfies the resonance condition maximizing the C-SPP transmission out of it, such that [8].

$$\mathrm{Re}(k_{csp})d - \varphi_{Trench} = 2m'\pi, \tag{2}$$

where d dentoes the distance between P_1 and P_1', φ_{Trench} the phase shift caused by the reflection at the trench wall, and m' an integer number.

Here, two different types of TA-CMNSs are under consideration [8]: One is a rectangular trench (RT) and the other is an asymmetric parabolic trench (APT). While the RT-CMNS has a merit in terms of ease of fabrication, one can improve the SNR performance more significantly with the APT-CMNS because it facilitates increasing the charge concentration at P_2 relative to P_1 [8, 20]. All the detailed parameters can be optimized via iterative numerical procedures as discussed in [8].

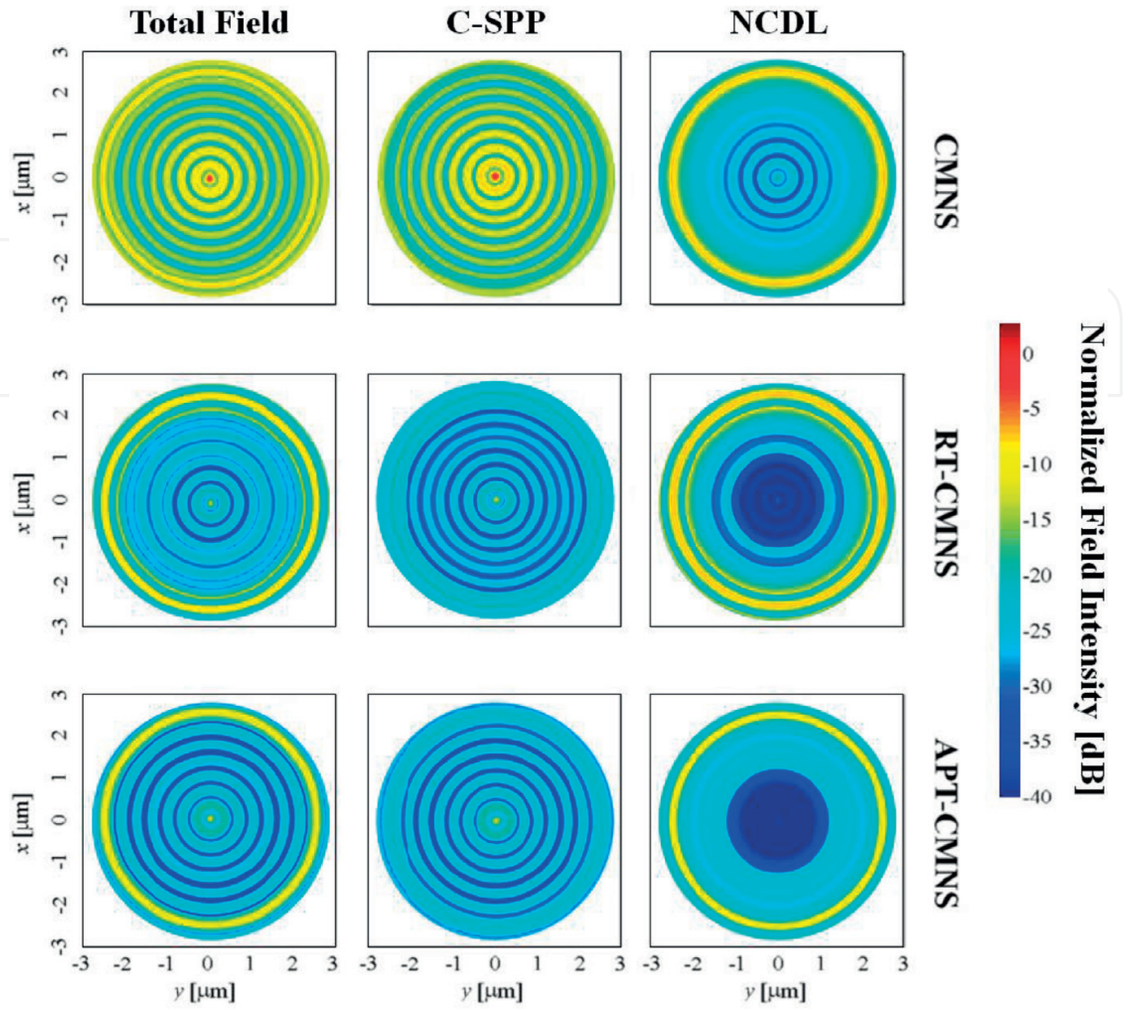

Figure 4. Top views of the total, plasmonic, and NCDL field intensity distributions [8].

Figure 4 illustrates the field intensity distributions of the total field, the C-SPP, and the NCDL for the CMNSs with no trench structure and the optimized RT and APT structures, respectively [8]. From the figure, one can observe that there are clear differences among the simple CMNS and the TA-CMNSs in terms of the NCDL suppression characteristics. With the TA structures, the NCDL noises were substantially canceled out at the center of the device. In particular, the peak and mean SNRs could reach 50.71 and 36.03 dB, respectively, for the APT-CMNS, which were more than one order of magnitude higher than those of the simple CMNS. The peak and mean SNRs of all the three devices are summarized in **Table 1**.

	CMNS (dB)	RT-CMNS (dB)	APT-CMNS (dB)
Peak SNR	34.27	38.58	50.71
Mean SNR	24.14	31.11	36.03

Table 1. Summary of the SNR values estimated within the main lobe of the C-SPP hotspots [8].

3. Fiberized plasmonic Fresnel zone plates

Focusing light is invariably an important issue for numerous applications, including micro-machining [23], optical tweezing [24, 25], bio-sensing [26, 27], etc. In particular, easy and accurate control of the focal point is one of the greatest factors to be considered for focusing apparatus from the perspective of practical implementation. A traditional method for shifting the focal point is to move either the focusing lens or the target object. Such mechanical adjustments tend to result in relatively large inaccuracies, which are undesirable by any means.

Recently, the author has proposed and demonstrated a simple and compact micro/nanophotonic structure combining fiber-optic and metal-optic technologies in order for super-variable focusing of light [9], where the relatively high chromatic aberration properties of flat-metal-optical lenses were exploited for an alternative measure of varying its focal point in a wide range.

In this section, the author discusses the characteristics of metallic Fresnel zone plate (FZP/MFZP) structures implemented on a metal-coated optical fiber facet, that is, metallic Fresnel-zone-plated optical fiber facets (MFZP-OFFs), and shows that they can have novel super-variable focusing functionality [9]. Moreover, the author discusses another SPP-based MFZP-OFF scheme that can selectively focus light, depending on its polarization state [9, 28]. In particular, this novel SPP-based lens can be useful for some specific applications that inevitably require centrosymmetric optical force, such as optical trapping [29] and micro-machining [30].

3.1. MFZP-OFFs for super-variable focusing of light

The focal position of a conventional lens, such as spherical lens, varies mainly by the chromatic dispersion of the lens material. For example, the focal length of a bi-convex lens is given by [31].

$$f = \frac{R_1 R_2}{R_2 - R_1} \frac{1}{n_{lens} - 1}, \tag{3}$$

where f denotes the focal length, R_1 and R_2 the radii of the curvatures of both lens facets, and n_{lens} the optical refractive index of the lens material. In general, the chromatic dispersion of n_{lens} is given by a value in the order of $\sim 10^{-5}$/nm for fused silica [32], so that it results in a very limited focal length change with respect to incident wavelength. In contrast, a flat-metal-optical lens based on an FZP exhibits a drastically different aspect because the focusing of light is obtained from the constructive interference of light at a location where all the possible optical paths from the annular openings of the FZP become in phase, so that detuning of the condition is caused not by the material dispersion but by the direct change of the wavelength of incident light [31, 33].

In general, the product of the focal length and the incident wavelength is approximately invariant regardless of the given FZP geometry [9, 33], so that the general expression for the focal length f_λ as a function of the incident wavelength λ can be given by

$$f_\lambda \approx \frac{\lambda_0 f_0}{\lambda}, \tag{4}$$

where λ_0 and f_0 denote the reference wavelength and focal length, respectively. It shows that an FZP has a focal length that is inversely proportional to the incident optical wavelength. In addition, one can also notice that the beam radius at the focal point of an FZP, that is, r_r^2 tends to remain nearly consistent regardless of the incident wavelength, considering the optical diffraction principle [9, 31] such as

$$r_{e^2} \propto \frac{1}{kNA} \approx \frac{\lambda f_\lambda}{2\pi R}, \tag{5}$$

where k, NA, and R denote the wavenumber of the incident light, the effective numerical aperture of the lens, and the radius of the lens, respectively. Since the product of the wavelength and the focal length remains invariant from Eq. (4), Eq. (5) indicates that the beam radius at the focal point of an FZP is approximately preserved regardless of the wavelength of the incident light.

On the other hand, MFZP-OFFs can readily be fabricated using electron-beam and evaporation and FIB milling techniques [34, 35]. **Figure 5** illustrates an MFZP-OFF fabricated in house based on the techniques and its focusing characteristics. Silver was initially deposited via an electron-beam evaporation system to form a 100-nm layer on the flat-cleaved multimode optical fiber facet. The multimode optical fiber had a 50-μm diameter step-index core with 0.22 NA. The silver layer was processed by FIB milling to have the FZP structure consisting of 6 rings [9]. It should be noted that this FZP was designed to produce a focal spot at 20 μm from the fiber facet when the wavelength of incident light was tuned at 550 nm.

To characterize the MFZP-OFF, visible light of three different colors (RGB) was launched into the other end of the optical fiber. The center wavelengths of them were given by 612 (R), 527 (G), 473 (B) nm, respectively. The focal length of the MFZP-OFF was measured by an optical

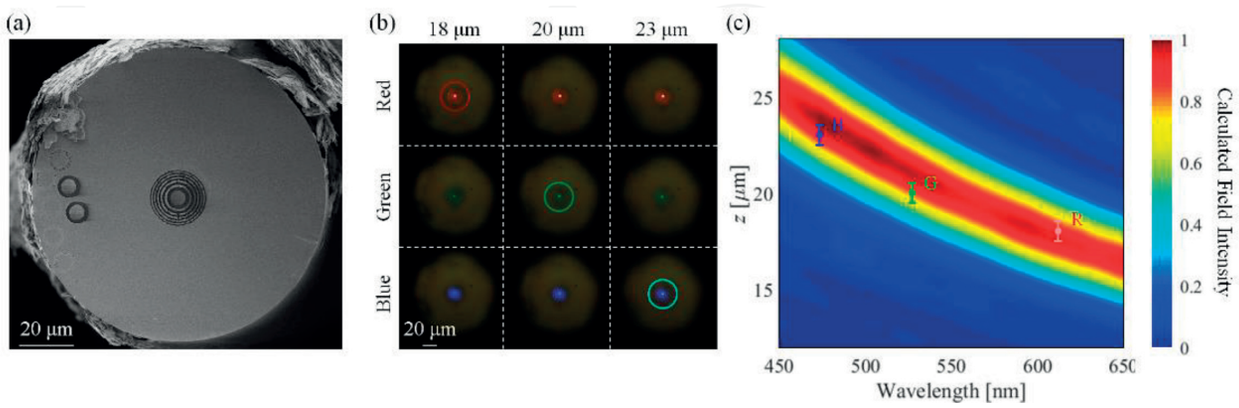

Figure 5. Experimental results of the fabricated MFZP-OFF [9]: (a) Scanning electron microscope (SEM) image of the fabricated MFZP-OFF. (b) Optical microscope images of the transmitted light at various incidence and distance conditions. (c) Numerical results on the normalized field intensity distributions along the z-axis with respect to the wavelength of incident light.

microscope system, and the measured focal points for RGB colors were at z = 18 (R), 20 (G), and 23 (B) μm, respectively. Numerical simulations were also performed to verify the experimental results, which are shown in **Figure 5(c)**. The numerically calculated focal points for RGB colors were given by z = 17.6 (R), 21.0 (G), and 23.8 (B) μm, respectively, which were actually in good agreement with the experimental results. In fact, the focal length of the MFZP-OFF varied from 28.6 to 14.9 μm for the wavelength range from 400 to 700 nm, which means the relative focal-length change per unit wavelength was as large as 45.5. It is highlighted that this relative change rate is over 20 times higher than the rate that can be obtained with a conventional silica-based lens [9, 31], as the latter can only be detuned from 20.2 to 19.6 μm for the same spectral detuning range. In addition, the mean beam radius averaged out over the whole visible range was calculated to be 768 nm with a standard deviation of 14.2 nm, which indicates that the relative change was only 1.84% over the whole visible range as expected from Eq. (5). Nevertheless, it should be noted that even though the super-variable focusing capability along with a nearly constant beam spot size at the focal point over the very wide spectral range was verified both numerically and experimentally, the depth of focus of the focal spot along the optical axis should still be inversely proportional to the wavelength of incident light [28, 33].

3.2. All-sub-wavelength-scaled MFZP

If all the openings of the standard MFZP discussed in the preceding section are reduced down into the sub-wavelength scale [9, 28], its transmission starts to be dominated by the SPP-mediated radiation, that is, the extraordinary optical transmission (EOT) via SPPs. Subsequently, such an MFZP (hereinafter SPP-MFZP) will bring in polarization-dependent characteristics because SPPs are normally excited in the direction perpendicular to the slit walls, so that only the radially polarized mode can lead to a hotspot. Thus, this SPP-MFZP can be utilized for focusing of radially polarized light, which has considerable advantages over the linearly polarized or un-polarized counterparts in various applications, thanks to its axially symmetric optical characteristics [30, 36]. The author has investigated the polarization-selective characteristics of the sub-wavelength-scale annular slit in [9], verifying that the transmission of azimuthally polarized (i.e., parallel-polarized) light was suppressed drastically if the relative slit width with respect to wavelength, that is, s/λ, was given by $< \sim 0.3$, while the transmission of radially polarized (i.e., perpendicular-polarized) light remained nearly unchanged.

Thus, building upon the principle, an SPP-MFZP was fabricated and characterized experimentally. A 195-nm-thickness gold layer was deposited on a fused-silica substrate, using the electron-beam evaporation method. A standard 6-ring FZP was designed for the reference wavelength of 660 nm and the reference focal length of 20-μm, and all the rings was filled with sub-wavelength-slits of a 120-nm width with a 50% duty ratio. **Figure 6(a)** illustrates the SEM image of the fabricated SPP-MFZP. To characterize its polarization-dependent functionality, linearly polarized light was illuminated on it. Rotating the axis of the incident polarization, its transmission through the SPP-MFZP was measured by the optical microscope. Considering that the linearly polarized light can be decomposed into a radial component and an azimuthal component with a different ratio depending on the location on the SPP-MFZP plane, the transmitted light pattern should be like a "figure of eight." **Figure 6(b)** illustrates the optical

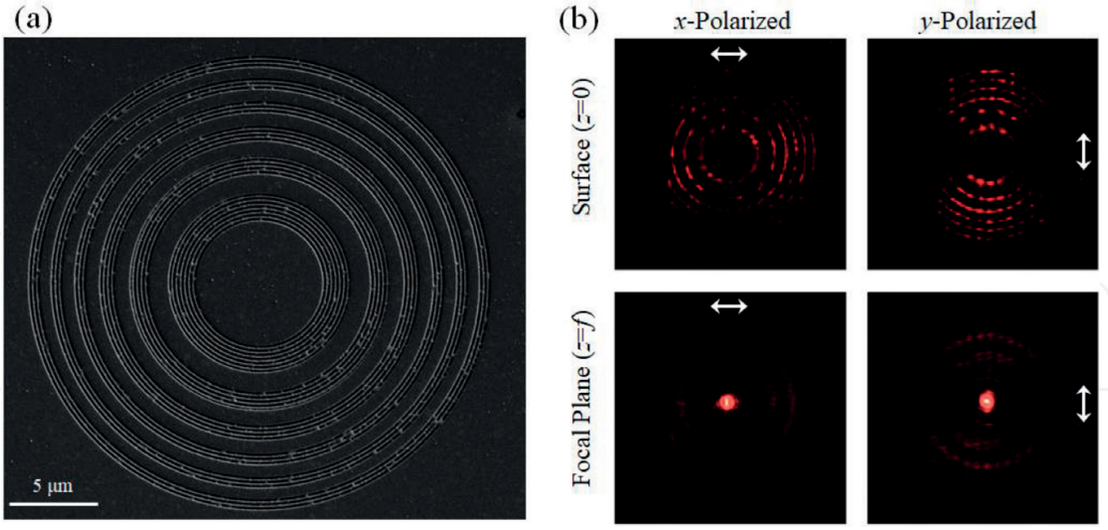

Figure 6. Experimental results of the fabricated SPP-MFZP [9]: (a) SEM image of the SPP-MFZP fabricated on a gold-coated fused-silica substrate. (b) Dark-field optical microscope images of the transmitted light at different image planes and for different incident polarization states.

microscope images of the transmitted light patterns at the top surface of the SPP-MFZP and at the focal plane for two different linear polarization states. The results suggest that the SPP-MFZP functioned as expected, such that only the radial-polarization mode could efficiently pass through the SPP-MFZP, being selectively focused down at the focal plane. It is noteworthy that the SPP-MFZP can readily be implemented onto a fiber facet in a way similar to the MFZP-OFF discussed in the preceding section.

4. Metal-coated angled optical fiber facets

Efficient excitation of SPPs is invariably important because SPPs cannot be excited naturally, which means it requires some specific apparatus leading to the special boundary condition at the dielectric-metal interface [37]. The prism coupling technique based on the Kretschmann configuration is one of the most frequently used methods for this purpose [37]. This technique utilizes an oblique incidence toward a dielectric-metal interface, in which the real part of the dielectric material should be higher than that of the metal. In optical fiber platforms, the technique was not fully exploited, such that SPPs were normally excited via using tip structures, nanoslits or apertures, the polished or tapered side of the optical fiber, etc. [4–7].

Recently, the author has introduced a novel SPP coupling scheme in the optical fiber platform that is based on a metal-coated angled fiber facet (MCAFF) different from the aforementioned conventional schemes [10]. In fact, this scheme exploited the so-called Kretschmann configuration on the optical fiber platform, because the angle fiber facet can play exactly the same role as a prism to the optical mode guided in the core of the fiber [10, 37].

In this section, the author discusses the MCAFF configuration with corresponding numerical and experimental results, and also shows how it can be utilized for further applications,

including a corrugation-assisted MCAFF for wavelength-dependent off-axis directional beaming. Unlike the conventional SPP-coupling techniques having trade-offs and limitations from various perspectives, such as efficiency, compactness, unidirectional coupling, alignment, etc., the MCAFF configuration can readily resolve the aforementioned issues, so that it can be an efficient alternative to the existing techniques.

4.1. SPP coupling scheme based on a metal-coated angled fiber facet

In general, optical-fiber-based SPP generation has mostly been done based on nanoslit structures [4, 6, 9, 38]. However, its coupling efficiency tends to be considerably low by the following factors: the generation of NCDL, the excitation of multidirectional SPPs, and the reflection of the incident light by aperture [10] as illustrated in **Figure 7(a)**. In fact, such issues can be overcome if the Kretschmann configuration [37] is directly exploited on an angled optical fiber facet as illustrated in **Figure 7(b)**.

In fact, the Kretschmann's prism coupling configuration should still be valid for an angled fiber facet, because it can be regarded as a prism to the optical mode guided in the core of the fiber [10, 37]. Subsequently, an MCAFF can excite SPPs along the dielectric-metal interface as long as the following phase-matching condition is satisfied [10]:

$$k_{SP0} = n_{eff}\, k_0\, sin\theta = k_0 \sqrt{\frac{\varepsilon_d \varepsilon_m}{\varepsilon_d + \varepsilon_m}}, \tag{6}$$

where k_0 denotes the wavenumber of the optical radiation in free space, k_{SP0} the wavenumber of the SPP, ε_d and ε_m the electric permittivities of the dielectric and the metal, respectively, n_{eff} the effective refractive index of the optical fiber mode, and θ the incidence angle of the optical

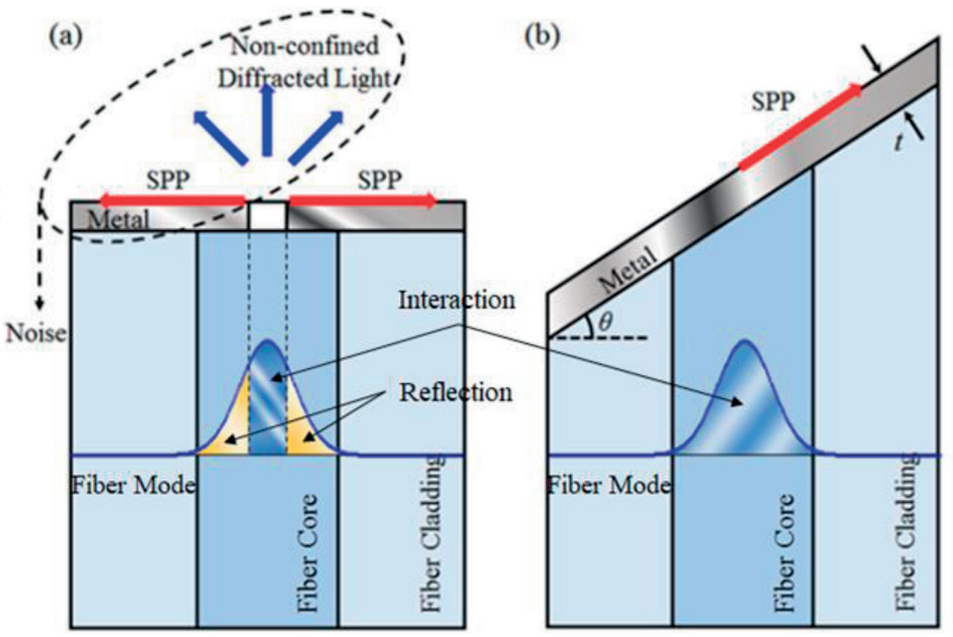

Figure 7. Fiber-SPP-mode coupling schemes [10]: (a) Nanoslit coupling scheme and (b) MCAFF scheme.

fiber mode relative to the fiber-metal interface or simply the angle of the optical fiber facet relative to the optical fiber axis as illustrated in **Figure 7(b)**.

In this scheme, two kinds of SPPs can be generated. One is the propagating SPP (P-SPP) mode that is the eigen mode of the given interface geometry, and the other is the localized SPP (L-SPP) mode directly induced by the incident wave [2, 10, 26, 37]. In order to verify the functional characteristics of the MCAPP, one can first perform numerical calculations of an example structure, assuming that the optical fiber is a step-index fiber with a core diameter of 3 μm and an NA of 0.1, and that the metal coating material is silver.

Figure 8(a) illustrates the field pattern of the MCAFF when the incident light was launched from the other end of the optical fiber, in which the metal thickness, the fiber-facet angle, and the incident wavelength were given by 20 nm, 45°, and 600 nm, respectively [38]. It should be noted that the incident optical fiber mode was assumed to be an x-polarized LP_{01} mode. From the figure, one can see that an SPP mode was dominantly generated at the top surface of the metal layer, and a fraction of the incident light was immediately reflected by the dielectric-metal interface, and some of the SPP mode was decoupled back into the dielectric region after some propagation length. In fact, the decoupled component can also give rise to loss to the P-SPP, which can be observed at the right-top-corner indicated by a round-rectangle in a dashed-line. This is different from the direct reflection of the optical mode around the core region, and it can be avoided if the metal thickness increases considerably [10]. With the metal thickness of 20 nm, the spectral SPP coupling efficiency in terms of the fiber-facet angle is illustrated in **Figure 8(b)**. The calculated efficiency reached close to 70% in the phase-matched condition. In addition, the given MCAFF structure showed a sufficiently broad spectral bandwidth covering the whole visible range with the given metal thickness of 20 nm. In fact, deciding the thickness of the metal layer is really dependent on the type of the application of the MCAFF. If the excitation of SPP is important only nearby the core region, one may choose a thin metal layer (~ 20 nm) to intensify the direct coupling. In contrast, if it requires a relatively long propagation length, one may go for a considerably thick metal layer (> 30 nm) in order to

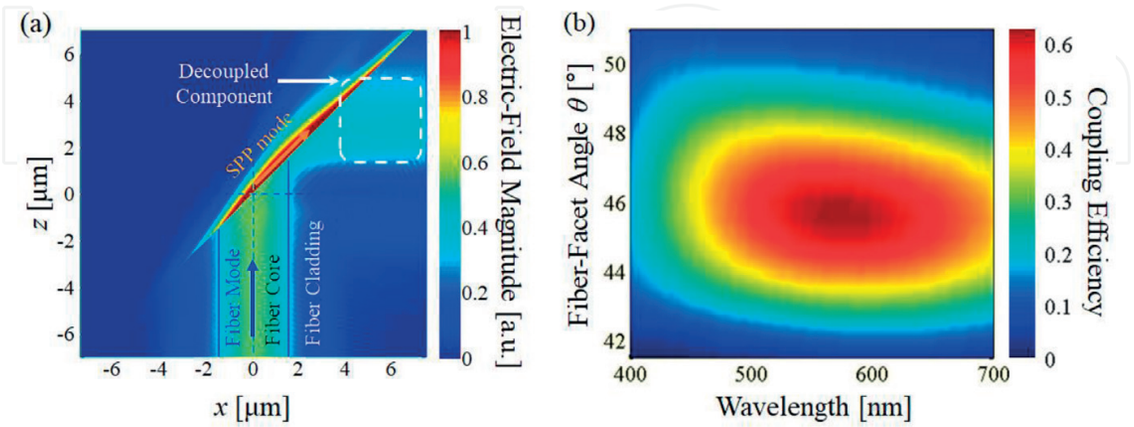

Figure 8. SPP coupling scheme based on the MCAFF [10]: (a) Field pattern of a specific MCAFF configuration. (b) Spectrum of the SPP coupling efficiency in terms of the fiber-facet angle and incident wavelength.

suppress the decoupling of the SPP. In the latter case one may also alternatively consider choosing a thin layer nearby the core region and gradually increasing the thickness of the metal layer outside the core region.

Figure 9(a) illustrates an experimental setup to characterize the MCAFF [39]. An angle-cleaved optical fiber end supported in the substrate was metal (silver)-coated based on the electron-beam evaporation method. The optical fiber had a step-index core of a 5.3 μm diameter and of an NA of 0.14. The facet angle and the wavelength of incident light were given by $\theta = 46^{\circ}$ and 650 nm, respectively. Two samples with different metal thicknesses of 20 and 30 nm were fabricated. In order to decouple the SPP excited on the MCAFF surface out to free space, the surface was roughly ground to have some randomized texture. In addition, the incident polarization state was controlled by the rotation of the input polarizer, and the transmitted light was monitored and imaged by an optical microscope with a complementary metal-oxide-semiconductor (CMOS) camera. It should be noted that the SPP mode can only be excited by a transverse-magnetic (TM) mode. Thus, one can expect that the out-coupled light could only be observed if a TM optical mode were incident onto the MCAFF. In contrast, a transverse-electric (TE) mode would undergo substantial attenuation, so that it would be hard to observe its transmission. The facet images detected by the CMOS camera are shown in **Figure 9(b)** for the two MCAFF samples in the TM and TE incidence conditions. One can clearly see that significantly brighter transmission was detected when TM-polarized light was launched than when TE-polarized light was launched. Moreover, significantly brighter transmission was detected from the 30-nm-thickness MCAFF than the 20-nm-thickness MCAFF, which was due to the fact that the thinner (∼ 20 nm) metal layer caused relatively larger decoupling loss than the thicker (∼ 30 nm) metal layer, because the SPP was allowed to propagate a relatively long distance in this case, as already discussed.

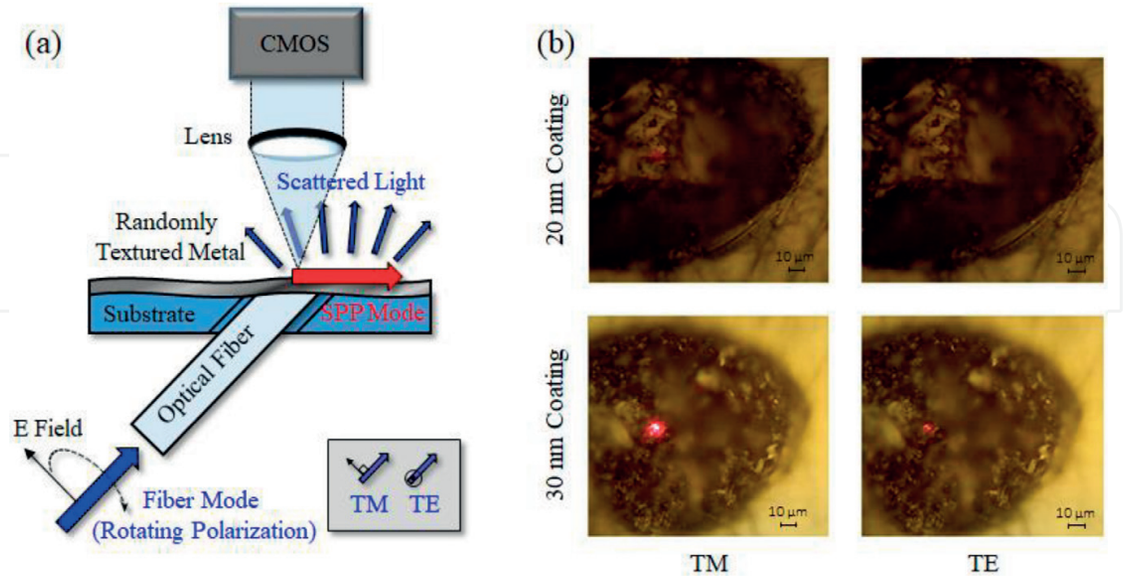

Figure 9. Experimental results of fabricated MCAFFs [39]: (a) Experimental arrangement for characterizing the fabricated MCAFFs. (b) Decoupled light from the MCAFFSs for incident light at 650 nm with different polarization modes.

4.2. Application of the MCAFF scheme: corrugation-assisted MCAFF for wavelength-dependent off-axis beaming

In this section, the author discusses a corrugation-assisted MCAFF (CA-MCAFF) structure, which has wavelength-dependent off-axis directional beaming (WODB) functionality [40–42]. The schematic of the CA-MCAFF is shown in **Figure 10**. It is noteworthy that the incident optical fiber mode can be coupled into both P-SPP and L-SPP at the top surface of the metal layer, which can be decoupled into free-space mode through the periodic corrugation structure depending on the phase-matching condition given by [10, 42]:

$$k_{SPP} \pm mk_c + k_0 \sin\phi = 0, \tag{7}$$

where k_{SPP} denotes the wavenumber of the SPP (either P-SPP or L-SPP), k_0 the wavenumber of the optical radiation in free space, k_c the reciprocal lattice vector (i.e., $k_c = 2\pi/\Lambda$) of the corrugation having a period of Λ and ϕ the azimuthal angle of the out-coupled optical radiation in free space relative to the surface-normal vector of the MCAFF as shown in **Figure 10(a)**. If the period of the corrugation Λ is fixed, the angle of the out-coupling ϕ will subsequently vary with wavelength [10, 42]. It is noteworthy that the L-SPP is excited owing to the localized plasmonic oscillation in the trough segment of the corrugation whereas the P-SPP is excited owing to the nonlocalized, normal SPP oscillation spread out along the whole metal-air interface of the periodical corrugation. Therefore, in the given condition, one can expect that the L-SPP will become the dominant mode rather than the P-SPP, because the latter will undergo significantly higher attenuation by ohmic loss in the metal than the former [37].

It is noteworthy that the CA-MCAFF requires high coupling efficiency nearby the core region, so that a thin metal layer of 20 nm should be a relevant choice. In addition, the initial fiber-facet angle θ and the duty ratio of the unit corrugation should also be determined carefully,

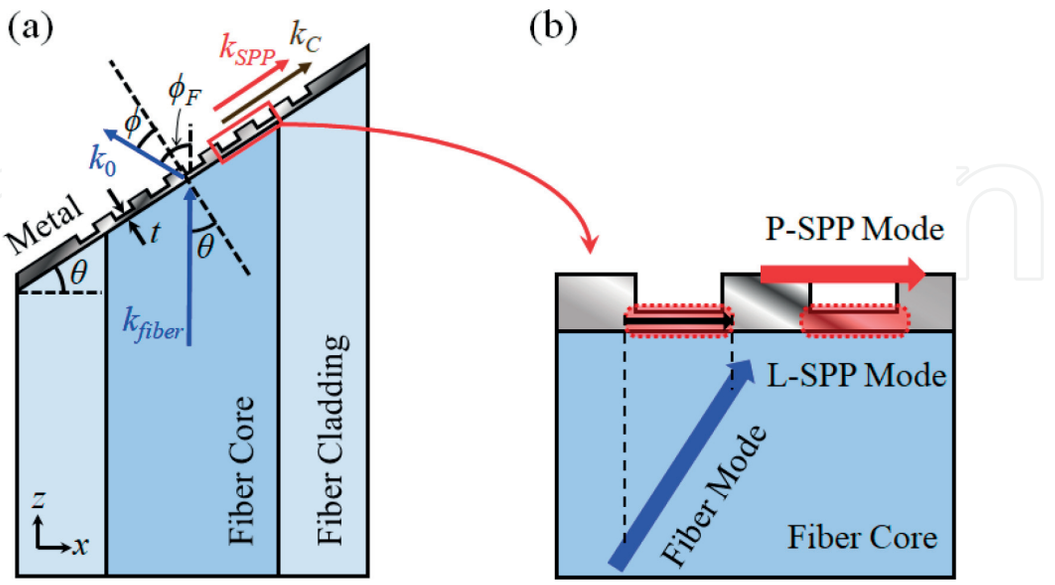

Figure 10. CA-MCAFF and its corresponding SPP modes [10]: (a) Schematic of the CA-MCAFF. (b) Two different types of SPP modes excited at the periodically corrugated metal surface.

depending on what characteristic of the CA-MCAFF is most desired, for example, the overall out-coupling efficiency, spectral bandwidth, etc. [10]. **Figure 11** illustrates the calculated far-field magnitude distribution through the CA-MCAFF, in which the thickness of the metal layer and the fiber-facet angle were set to 20 nm and 50°, respectively, and the period, modulation depth, and duty ratio of the corrugation were set to 380 nm, 40 nm, and 47%, respectively. These parameters were determined after going through iterative calculations from the perspective of maximizing the overall out-coupling efficiency [10]. In the figure, there are a few virtual lines drawn: The solid white line and dashed black line denote the theoretically calculated output beaming angles when phase-matched with the L-SPP and the P-SPP, respectively. As already explained that the L-SPP mode should be the dominant SPP mode in the given structure, one can see that the actual beaming angle was better fitted with the beaming angle trace by the L-SPP mode than with the trace by the P-SPP mode. In particular, higher out-coupling took places where both traces are matched or close to each other, which peaked at $\sim$ 500 nm as depicted in **Figure 11**. This means that the wavenumber of L-SPP and P-SPP was close to each other in the given condition, which eventually enhanced the aggregate coupling efficiency of the SPPs. In addition, it is noteworthy that the beaming angle exhibited good linearity with wavelength, which in fact justifies that the CA-MCAFF can efficiently be used for WODB. On the other hand, the dash-dotted blue and red lines represent the case when the incident fiber optical mode was phase matched with unwanted backward-propagating SPP modes, such as the SPP modes excited at the metal-fiber interface and the air-metal interface, respectively, for $m = -2$ in Eq. (7). The second-order coupling should be possible because the periodic corrugation was formed in an asymmetrically layered structure in the transverse (or vertical) direction [10]. When the main beaming line passed across these two traces, the out-coupling efficiency dropped a bit, because the phase-matching conditions for the L-SPP and for the backward-propagating SPPs were satisfied at the same time. However, this unwanted consequence had already been minimized while optimizing the duty ratio of the corrugation [10].

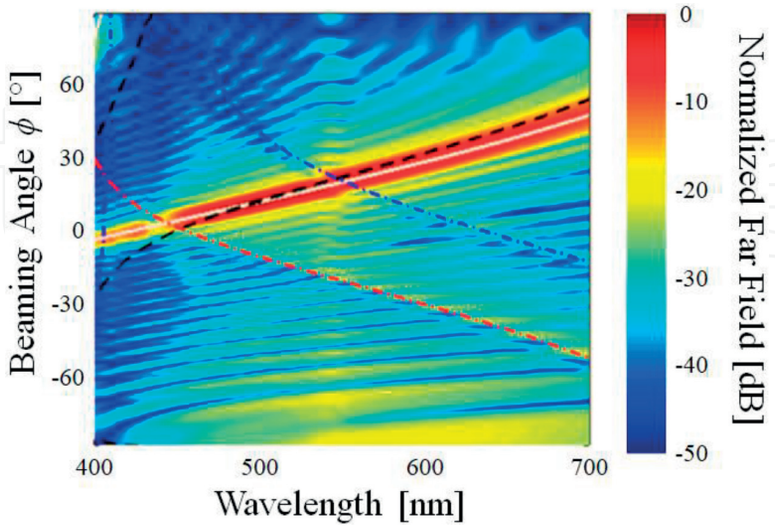

Figure 11. Numerical results of the far-field magnitude distribution and the analytical results of the primary beaming angle of the optical radiation from the CA-MCAFF with respect to the wavelength of incident light and the azimuthal angle ϕ [10].

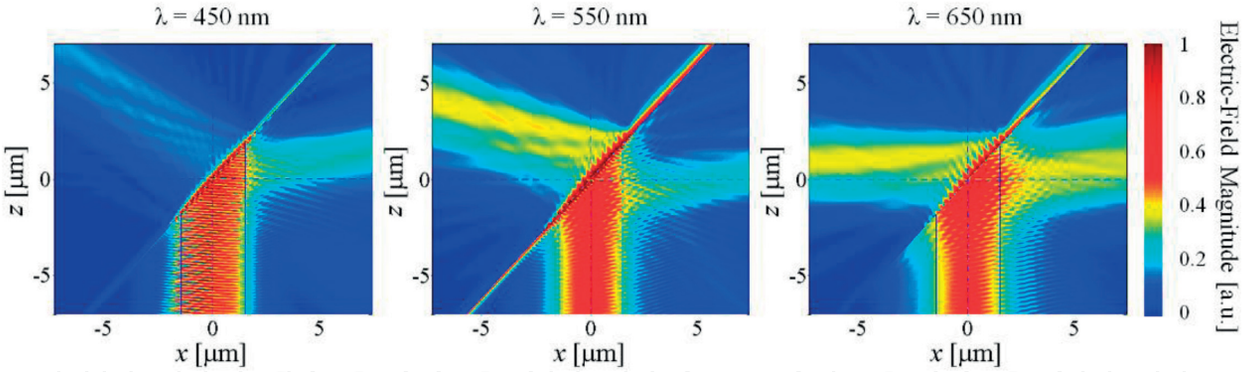

Figure 12. Field magnitude patterns of a specific CA-MCAFF for RGB incidence conditions [10].

Figure 12 illustrates the resultant field pattern nearby the core region for different incident wavelengths, which justifies the spatial beaming characteristics of the out-coupled optical radiation from the CA-MCAFF. It is clearly shown that the L-SPP mode was dominantly generated above the core region, and a fraction of it propagates along the air-metal interface and another fraction was out-coupled into free space. They show different beaming angles with incident wavelength, confirming the WODB characteristics. In particular, for 550 nm, one can see that the incident light was also coupled to the counter-directionally propagating SPP, which has also been denoted by the dash-dotted blue line in **Figure 11**. The overall out-coupling efficiency for WODB was estimated to be as high as 30% [10] for the given CA-MCAFF.

5. Conclusion

Throughout this chapter, the author has discussed novel plasmonic structures implemented on various optical fiber platforms. These fiber-optic-based plasmonic devices demonstrated novel features of SPP-based functionality in a compact, flexible, and cost-effective form leveraged by optical fiber technology.

First, fiberized TA-CMNSs that can produce a low-noise C-SPP hotspot were introduced and discussed. The trench structures were designed based on the MPCM in order to suppress the co-existing NCDL at the hotspot location. Two types of novel TA-CMNSs were designed and investigated: an RT-CMNS was proposed for its simple fabrication procedure, and an APT-CMNS was proposed for maximally exploiting the multipole cancelation effect. Numerical analysis of them verified that the auxiliary trench structure can substantially improve the SNR performance of the CMNS, being capable of producing a low-noise plasmonic hotspot at the center of the whole structure. These schemes will be useful for designing various plasmonic devices that particularly require high SNR characteristics, such as bio-sensing, imaging, surface-enhanced Raman spectroscopy, etc.

Second, fiberized and fiberizable metal-optical lenses based on the FZP were introduced and discussed, which included an MFZP-OFF and an SPP-MFZP. The former exhibited super-variable focusing with respect to incident wavelength, and the latter had substantially high

radial-polarization selectivity owing to the EOT effect from the auxiliary subwavelength annular slits inserted in the openings of the FZP structure. Numerical and experimental analyses verified their novel functionality. These schemes will be useful for various applications that require accurate, flexible, and centrosymmetric optical focusing with a broad focal-length tuning range, such as in micro/nanomachining and optical trapping. In addition, these schemes can also be exploited for mono-chromatic-multi-focal or multi-chromatic-mono-focal lenses [43, 44].

Third, a fiberized SPP coupling scheme and its application to a CA-MCAFF were introduced and discussed. The former realized the Kretschmann SPP coupling scheme in the optical fiber platform, and the latter exhibited novel WODB functionality. Numerical and experimental analyses verified that the MCAFF-based SPP coupling scheme worked efficiently and has great potential for being used as an excellent, alternative SPP generation method, which provides high efficiency, unidirectionality, and full compatibility with fiber-based optical sources. The CA-MCAFF scheme will also be very useful for various plasmonic and optical applications where WODB functionality is required, such as a nanophotonic wavelength-division-multiplexer, a compact spectrometer, etc.

Optical fibers are an excellent platform for plasmonics studies and applications. The novel plasmonic nanostructures realized on various optical fiber platforms successfully demonstrated fascinating characteristics of plasmonics in a compact, flexible, and cost-effective format. The author believes that the investigations and discussions given in this chapter will broaden the fiber-optic and plasmonics research fields, as well as expecting further advances and convergence of them to come.

Acknowledgements

The author acknowledges the useful discussion with Prof. Y. Jeong.

Author details

Hyuntai Kim

Address all correspondence to: H.Kim@soton.ac.uk

Optoelectronics Research Centre, University of Southampton, Southampton, United Kingdom

References

[1] Ghatak A, Thyagarajan K. An Introduction to Fiber Optics. Cambridge: Cambridge University Press; 1998

[2] Agrawal G. Nonlinear fiber optics. San Diego, California: Academic Press; 1995

[3] Alwayn V. Optical Network Design and Implementation. Indianapolis: Cisco Press; 2004

[4] Guan C, Ding M, Shi J, Wang P, Hua P, Yuan L, Brambilla G. Compact all-fiber plasmonic Airy-like beam generator. Optics Letters. 2014;**39**(5):1113-1116

[5] Lin Y, Guo J, Lindquist RG. Demonstration of an ultra-wideband optical fiber inline polarizer with metal nano-grid on the fiber tip. Optics Express. 2009;**17**(20):17849-17854

[6] Kostovski G, Stoddart PR, Mitchell A. The optical fiber tip: An inherently light-coupled microscopic platform for micro-and nanotechnologies. Advanced Materials. 2014;**26**(23): 3798-3820

[7] Mullen KI, Carron KT. Surface-enhanced Raman spectroscopy with abrasively modified fiber optic probes. Analytical Chemistry. 1991;**63**(19):2196-2199

[8] Kim H, Lee S-Y, Koo S, Kim J, Park K, Lee D, Vazquez-Zuniga LA, Park N, Lee B, Jeong Y. Theoretical study on the generation of a low-noise plasmonic hotspot by means of a trench-assisted circular nano-slit. Optics Express. 2014;**22**(22):26844-26853

[9] Kim H, Kim J, An H, Lee Y, Lee G-y, Na J, Park K, Lee S, Lee S-Y, Lee B, Jeong Y. Metallic Fresnel zone plate implemented on an optical fiber facet for super-variable focusing of light. Optics Express. 2017;**25**(24):30290-30303

[10] Kim H, An H, Kim J, Lee S, Park K, Lee S, Hong S, Vazquez-Zuniga LA, Lee S-Y, Lee B, Jeong Y. Corrugation-assisted metal-coated angled fiber facet for wavelength-dependent off-axis directional beaming. Optics Express. 2017;**25**(7):8366-8385

[11] Srituravanich W, Pan L, Wang Y, Sun C, Bogy DB, Zhang X. Flying plasmonic lens in the near field for high-speed nanolithography. Nature Nanotechnology. 2008;**3**(12):733-737

[12] Kim S, Jin J, Kim Y-J, Park I-Y, Kim Y, Kim S-W. High-harmonic generation by resonant plasmon field enhancement. Nature. 2008;**453**(7196):757-760

[13] Moh K, Yuan X-C, Bu J, Zhu S, Gao BZ. Radial polarization induced surface plasmon virtual probe for two-photon fluorescence microscopy. Optics Letters. 2009; **34**(7):971-973

[14] Radko IP, Bozhevolnyi SI, Evlyukhin AB, Boltasseva A. Surface plasmon polariton beam focusing with parabolic nanoparticle chains. Optics Express. 2007;**15**(11):6576-6582

[15] Lerman GM, Yanai A, Levy U. Demonstration of nanofocusing by the use of plasmonic lens illuminated with radially polarized light. Nano Letters. 2009;**9**(5):2139-2143

[16] Kinkhabwala A, Yu Z, Fan S, Avlasevich Y, Müllen K, Moerner W. Large single-molecule fluorescence enhancements produced by a bowtie nanoantenna. Nature Photonics. 2009; **3**(11):654-657

[17] Ropers C, Neacsu C, Elsaesser T, Albrecht M, Raschke M, Lienau C. Grating-coupling of surface plasmons onto metallic tips: A nanoconfined light source. Nano Letters. 2007;**7**(9): 2784-2788

[18] Kihm H, Kang J, Kyoung J, Lee K, Seo M, Ahn K. Separation of surface plasmon polariton from nonconfined cylindrical wave launched from single slits. Applied Physics Letters. 2009;**94**(14):141102

[19] Johnson SG, Fan S, Mekis A, Joannopoulos J. Multipole-cancellation mechanism for high-Q cavities in the absence of a complete photonic band gap. Applied Physics Letters. 2001; **78**(22):3388-3390

[20] Kim H, Koo S, Park N, Kihm H-w, Kim D. Application of multi-pole cancellation theory for the enhancement of signal to noise ratio of nano-slit-excited surface plasmon waves. In: SPP5; 2011

[21] Kim H, Kwon Y, Vazquez-Zuniga LA, Jeong Y. Rigorous analysis on a U-shaped index fiber for generating cylindrical vector beams in an all-fiber format. In: Opto-Electronics and Communications Conference (OECC). IEEE; 2012

[22] Chen W, Abeysinghe DC, Nelson RL, Zhan Q. Plasmonic lens made of multiple concentric metallic rings under radially polarized illumination. Nano Letters. 2009;**9**(12):4320-4325

[23] Venkatakrishnan K, Tan B. Interconnect microvia drilling with a radially polarized laser beam. Journal of Micromechanics and Microengineering. 2006;**16**(12):2603

[24] Ribeiro RSR, Dahal P, Guerreiro A, Jorge PA, Viegas J. Fabrication of Fresnel plates on optical fibres by FIB milling for optical trapping, manipulation and detection of single cells. Scientific Reports. 2017;**7**(1):4485

[25] Neuman KC, Block SM. Optical trapping. The Review of Scientific Instruments. 2004; **75**(9):2787-2809

[26] Spillman W, Patriquin D, Crowne D. Fiber optic linear displacement sensor based on a variable period diffraction grating. Applied Optics. 1989;**28**(17):3550-3553

[27] Aydin K, Seliga T, Balaji V. Remote sensing of hail with a dual linear polarization radar. Journal of Climate and Applied Meteorology. 1986;**25**(10):1475-1484

[28] Kim H, Kim J, An H, Park K, Jeong Y. Subwavelength ring assisted Fresnel zone plate for radially polarized light focusing. In: Lasers and Electro-Optics Pacific Rim (CLEO-PR). IEEE; 2017

[29] Rohrbach A, Stelzer EH. Trapping forces, force constants, and potential depths for dielectric spheres in the presence of spherical aberrations. Applied Optics. 2002;**41**(13):2494-2507

[30] Dorn R, Quabis S, Leuchs G. Sharper focus for a radially polarized light beam. Physical Review Letters. 2003;**91**(23):233901

[31] Saleh B, Teich M. Fundamental of Photonics. New York: John Wiley & Sons; 1991

[32] Malitson I. Interspecimen comparison of the refractive index of fused silica. Journal of the Optical Society of America. 1965;**55**(10):1205-1209

[33] Young M. Zone plates and their aberrations. Journal of the Optical Society of America. 1972;**62**(8):972-976

[34] Tomiyasu B, Fukuju I, Komatsubara H, Owari M, Nihei Y. High spatial resolution 3D analysis of materials using gallium focused ion beam secondary ion mass spectrometry (FIB SIMS). Nuclear Instruments and Methods in Physics Research Section B: Beam Interactions with Materials and Atoms. 1998;**136**:1028-1033

[35] Vesseur EJR, De Waele R, Lezec H, Atwater H, De Abajo FG, Polman A. Surface plasmon polariton modes in a single-crystal Au nanoresonator fabricated using focused-ion-beam milling. Applied Physics Letters. 2008;**92**(8):083110

[36] Zhan Q. Trapping metallic Rayleigh particles with radial polarization: Reply to comment. Optics Express. 2012;**20**(6):6058-6059

[37] Maier SA. Plasmonics: Fundamentals and Applications. New York: Springer Science & Business Media; 2007

[38] Kim H, Lee S-Y, Lee S, Lee B, Jeong Y. Plasmonic Grating-Assisted Nano-Slit Implemented in an all-Fiberized Format for Wavelength-Dependent Beaming. In: Advanced Solid State Lasers. OSA; 2014

[39] Kim H, Lee Y, An H, Vazquez-Zuniga LA, Lee B, Jeong Y. Metal-coated angled fiber facet for surface plasmon generation. In: Asia-Pacific Laser Symposium (APLS). OSK; 2016

[40] Lakowicz JR, Malicka J, Gryczynski I, Gryczynski Z. Directional surface plasmon-coupled emission: A new method for high sensitivity detection. Biochemical and Biophysical Research Communications. 2003;**307**(3):435-439

[41] Kim S, Kim H, Lim Y, Lee B. Off-axis directional beaming of optical field diffracted by a single subwavelength metal slit with asymmetric dielectric surface gratings. Applied Physics Letters. 2007;**90**(5):051113

[42] Yu L-B, Lin D-Z, Chen Y-C, Chang Y-C, Huang K-T, Liaw J-W, Yeh J-T, Liu J-M, Yeh C-S, Lee C-K. Physical origin of directional beaming emitted from a subwavelength slit. Physical Review B. 2005;**71**(4):041405

[43] Kim J, Kim J, Na J, Jeong Y. Numerical study of a novel bi-focal metallic Fresnel zone plate having shallow depth-of-field characteristics. Current Optics and Photonics. 2018;**2**(2): 147-152

[44] Kim J, Kim H, Lee G-Y, Kim J, Lee B, Jeong Y. Numerical and experimental study on multi-focal metallic Fresnel zone plates designed by the phase selection rule via virtual point sources. Applied Sciences. 2018;**8**(3):449